Structural Behavior and Raman Spectra of Perovskite-Like Solid Solutions $(1 - x)LaMg_{0.5}Ti_{0.5}O_{3-x}La_{2/3}TiO_3$

Igor Levin,* Terrell A. Vanderah, Tammy G. Amos, and James E. Maslar

National Institute of Standards and Technology, Gaithersburg, Maryland 20899

Received December 22, 2004. Revised Manuscript Received April 5, 2005

Structural behavior and phase transitions in the A-cation deficient perovskite-like solid solutions $(1 - x)LaMg_{0.5}Ti_{0.5}O_{3-x}La_{2/3}TiO_3$ ($0 \le x \le 0.5$) were studied to reveal crystal-chemical factors associated with the marked variation of dielectric properties with *x*-value. Structures and phase transisitons were characterized using variable-temperature transmission electron microscopy (TEM) and X-ray powder diffraction combined with ambient temperature neutron powder diffraction measurements. The solid solutions feature a series of octahedral-tilting phase transitions and a B-site Mg/Ti order−disorder phase transition; the temperatures of these transitions decreased with increasing *x*. Additionally, short-range ordering of A-site vacancies was detected for $x > 0.40$ using high-resolution TEM. The reported compositional dependence of the dielectric response was found to correlate with changes in octahedral tilting, B-site ordering, and short-range ordering of A-site vacancies. A phase diagram summarizing ordering and displacive phase transitions was determined from variable-temperature diffraction and imaging experiments. Among the tilting transitions, a relatively uncommon first-order phase transition between structures exhibiting orthorhombic ($a^+b^-b^-$ and $a^0b^-c^-$) and rhombohedral ($a^-a^-a^-$) tilt systems was observed; the rhombohedral tilt was stabilized at room temperature for $x = 0.50$. Raman spectra of the solid solutions revealed previously unreported anomalous asymmetric broadening of certain peaks associated with B-site ordering. This broadening, which occurred even for the samples exhibiting significant long-range Mg/Ti order and large anti-phase ordered domains, was attributed to a decreasing phonon correlation length caused by strong heterogeneity of the B-site order parameter within each anti-phase domain.

Introduction

Complex $La_{2/3}TiO_3$-based solid solutions crystallizing with perovskite-like structures have received considerable attention both as potential candidates for dielectric resonators used in wireless communications[1−5] and because of their interesting structural behavior associated with the ordering of A-site vacancies.[6,7] Recent studies[8] of phase equilibria in the quaternary $La_2O_3-TiO_2-MgO-CaO$ system revealed hitherto unreported perovskite solid solutions in the quasibinary section $(1 - x)LaMg_{0.5}Ti_{0.5}O_{3-x}La_{2/3}TiO_3$ which occur according to formula $La_{1-x/3}\square_{x/3}[Mg_{(1-x)/2}Ti_{(1+x)/2}]O_3$ ($0 \le x \le 0.5$). The $x = 0$ member $LaMg_{0.5}Ti_{0.5}O_3$ crystallizes with a monoclinic $P2_1/n$ perovskite-like structure having lattice parameters $a \approx \sqrt{2}a_c$, $b \approx \sqrt{2}a_c$, $c \approx 2a_c$, $\beta \approx 90°$ (where $a_c \approx 4$ Å refers to the ideal cubic perovskite cell);[9] this structure features NaCl-type (1:1) ordering of Mg and Ti on the B-sites superimposed onto the octahedral tilting $a^+b^-b^-$. The other end-compound, $La_{2/3}TiO_3$ ($x = 1$), is unstable in the pure form but can be stabilized by small substitutions on either A- or B-sites.[10] The stabilized $La_{2/3}TiO_3$ structure features ordering of La-occupied and vacant A-sites combined with $a^-b^0c^0$ octahedral tilting so that the resulting structure is orthorhombic *Cmmm* with the unit cell $2a_c \times 2a_c \times 2a_c$ (the chemical ordering vector is parallel to the $[001]_c$ direction and perpendicular to the octahedra tilting axis).[11] $LaMg_{0.5}Ti_{0.5}O_3$ exhibits a dielectric constant $\epsilon \approx 27$ and a temperature coefficient of resonant frequency $\tau_f \approx -82$ ppm/°C, whereas for $La_{2/3}TiO_3$, $\epsilon \approx 90$ and $\tau_f \approx +190$ ppm/°C.[8] In the solid solutions $La_{1-x/3}\square_{x/3}[Mg_{(1-x)/2}Ti_{(1+x)/2}]O_3$, ϵ increases and τ_f becomes more positive with increasing *x* yielding temperature-stable ($\tau_f = 0$) ceramics with $\epsilon = 48$ at $x \approx 0.47$.[5,8] Interestingly, the compositional dependences of ϵ and τ_f exhibit a break in slope with both properties abruptly more sensitive to composition for $x > 0.40$.[8] Crystal-chemical considerations suggest that increasing the Ti/Mg ratio in the solid solutions will reduce the temperatures of B-cation order−disorder and octahedral-tilting phase transitions. Additionally, ordering of La-vacancies can occur for

* To whom correspondence should be addressed. Tel: 301-975-6142. Fax: 301-975-5334. E-mail: igor.levin@nist.gov.

(1) Yoshioka, H. *Jpn. J. Appl. Phys. P2* **1994**, *33* (7A), L945−948.
(2) Kim, I. S.; Jung, W. H.; Inaguma, Y.; Itoh, M. *Mater. Res. Bull.* **1995**, *30* (3), 303−316.
(3) Suvorov, D.; Valant, M.; Skapin, S.; Kolar, D. *J. Mater. Sci.* **1998**, *33* (1), 85−89.
(4) Moon, J. H.; Park, H. S.; Lee, K. T.; Choi, J. H.; Yeo, D. H.; Yoon, S. J.; Kim, H. J. *Jpn. J. Appl. Phys., P1* **1997**, *36* (11), 6814−6817.
(5) Salak, A. N.; Seabra, M. P.; Ferreira, V. M. *J. Eur. Ceram. Soc.* **2003**, *23* (14), 2409−2412.
(6) Howard, C. J.; Lumpkin, G. R.; Smith, R. I.; Zhang, Z. M. *J. Solid State Chem.* **2004**, *177* (8), 2726−2732.
(7) Battle, P. D.; Bennett, J. E.; Sloan, J.; Tilley, R. J. D.; Vente, J. F. *J. Solid State Chem.* **2000**, *149* (2), 360−369.
(8) Vanderah, T. A.; Miller, V. L.; Levin, I.; Bell, S. M.; Negas, T. *J. Solid State Chem.* **2004**, *177*, 2023−2038.
(9) Avdeev, M.; Seabra, M. P.; Ferreira, V. M. *J. Mater. Res.* **2002**, *17* (5), 1112−1117.
(10) Abe, M.; Uchino, K. *Mater. Res. Bull.* **1974**, *9*, 147.
(11) Howard, C. J.; Zhang, Z. *Acta Crystallogr.* **2004**, *B60*, 249−251.

10.1021/cm040389f CCC: $30.25
Published on Web 05/18/2005

larger x-values. Both cation ordering and octahedral tilting are known[12,13] to have a strong effect on the dielectric properties of perovskites, and therefore could contribute to the anomalous compositional dependences of ϵ and τ_f. In the present study we applied transmission electron microscopy combined with X-ray and neutron powder diffraction to elucidate the detailed structural behavior in the solid solutions $La_{1-x/3}\square_{x/3}[Mg_{(1-x)/2}Ti_{(1+x)/2}]O_3$.

Experimental Section

Polycrystalline specimens of $La_{1-x/3}\square_{x/3}[Mg_{(1-x)/2}Ti_{(1+x)/2}]O_3$ solid solutions ($x = 0$, 0.10, 0.30, 0.40, 0.48, and 0.50) were prepared by solid-state reactions using La_2O_3 (99.99%, dried at 850 °C immediately prior to weighing), $CaCO_3$ (99.99%), $MgCO_3$ (high-purity, preanalyzed by thermogravimetric analysis), and TiO_2 (phosphate-free). Prior to each heat-treatment, samples were ground with an agate mortar and pestle for 15 min, pelletized, and placed on sacrificial powder of the same composition on Pt foil supported by alumina ceramic. After an initial overnight calcine at 950 °C, multiple 2−7-d heatings (with intermediate grinding and re-pelletizing) were carried out at 1450 °C. Samples were furnace-cooled to 700 °C and then air-quenched on the benchtop. Typically, 4−5 heatings were required to attain equilibrium, which was presumed when no further changes could be detected in the weakest peaks observed in the X-ray powder diffraction patterns. Selected samples in welded Pt capsules were quenched in water from various temperatures to determine the Mg/Ti order−disorder transition temperatures.

Room-temperature X-ray diffraction patterns for structural analyses were collected using a Siemens D500 $\theta-2\theta$ powder diffractometer equipped with a Ge monochromator and a position-sensitive detector. (The identification of any commercial product or trade name does not imply endorsement or recommendation by the National Institute of Standards and Technology). Cu$K\alpha_1$ radiation was used. The patterns were analyzed using commercial MDI Jade software. In-situ variable-temperature X-ray diffraction measurements were conducted using a Siemens D5000 $\theta-\theta$ diffractometer equipped with a high-temperature furnace and a position sensitive detector. For these experiments, Cu$K\alpha$ radiation was used. The samples for the high-temperature studies were prepared by depositing a thin layer of ceramic powder (ground as an ethanol slurry) on a Pt heating strip.

Samples for transmission electron microscopy were prepared using conventional grinding, dimpling, and ion thinning. Electron diffraction and diffraction contrast studies were carried out in a Philips EM 430 TEM operated at 200 kV and equipped with Gatan cooling/heating stages for in situ variable-temperature studies. A high-resolution JEOL 3010 UHR transmission electron microscope operated at 300 kV with a point-to-point resolution of 1.7 Å was used for structural imaging. Phase contrast simulations were performed using both Bloch wave and multi-slice calculations implemented in the Java script version of the EMS code.

Neutron powder diffraction data for Rietveld analysis were collected on the BT-1 diffractometer at the Center for Neutron Research at the National Institute of Standards and Technology, using a Cu(311) monochromator with a wavelength of 1.5402(2) Å, and an array of 32 He-3 detectors at 5° intervals. Collimation of 15, 20, and 7 arc minutes were used before and after the monochromator, and after the sample, respectively. Vanadium sample containers were used. Diffraction data were collected over a 2θ range of 3−168° with a step size of 0.05°. The general analysis system (GSAS) software package was used for Rietveld structural refinements.[14] Refined parameters included scale factor, background coefficients (Chebyschev polynomial), profile coefficients (pseudo-Voigt, GSAS type 3 function), positional parameters, B-site occupancies, and thermal displacement parameters.

Raman scattering was excited using 488-nm radiation from an argon ion laser and instrumentation that included a holographic notch filter, a 0.5-m focal length imaging spectrograph, and a back-illuminated, charge-coupled device camera system (ca. 2.4 cm^{-1} fwhm instrumental band-pass). Laser radiation was focused onto the powder to produce an approximately 230-μm diameter spot with a corresponding power density of about 26 W/cm^2. Intensities were corrected for the wavelength-dependent response of the optical system using a white-light source of known relative irradiance.

Results and Discussion

1. Structural Behavior at Room-Temperature. *X-ray and Electron Diffraction.* X-ray diffraction patterns for all samples with $x \leq 0.48$ could be indexed with unit cells analogous to pseudo-orthorhombic $LaMg_{0.5}Ti_{0.5}O_3$. In contrast, the diffraction pattern of the sample with $x = 0.50$ (Figure 1) exhibits a clear signature of a rhombohedral distortion and can be indexed according to a rhombohedral unit cell with lattice parameters $a \approx \sqrt{2}a_c$ and $\alpha \approx 60°$. The intensities of superlattice reflections $^1/_2hk0_c$ (h, $k = 2n + 1$) and $^1/_2hk0_c$ ($h = 2n + 1$, $k = 2n$) decrease markedly with increasing x and vanish for $x > 0.40$. The intensities of the $^1/_2hkl_c$ (h, k, $l = 2n + 1$) reflections also decrease significantly on going from $x = 0$ to $x = 0.30$ but retain nonzero values for the entire range of solid solutions up to $x = 0.50$ (Figure 1).

Figure 2 summarizes representative selected area electron diffraction patterns recorded in the $\langle 110\rangle_c$ and $\langle 001\rangle_c$ zone axis orientations for the samples having x-values ranging from 0 to 0.50 (all annealed at 1475 °C). The microstructures of all samples contained twin-type domains, and the diffraction patterns presented in Figure 2 all correspond to single domains. The intensities of the superlattice reflections at $^1/_2hk0_c$ ($h = 2n + 1$, $k = 2n$) decrease rapidly with increasing x. These reflections exhibit anisotropic broadening which is revealed by the linear streaks of diffuse intensity along the $[001]_o$ (subscript "o" refers to the $\sqrt{2}a_c \times \sqrt{2}a_c \times 2a_c$ orthorhombic cell) direction. The appearance of $^1/_2hk0_c$ ($h = 2n + 1$, $k = 2n$) reflections changes drastically for $x > 0.4$: the $[001]_o$-type streaking is replaced by the relatively isotropic broadening and the reflections become very weak and diffuse. Furthermore, for $x < 0.4$, each single twin domain generated one set of the $^1/_2hk0_c$ ($h = 2n + 1$, $k = 2n$) reflections only, whereas for $x > 0.4$, each domain yielded two sets (Figure 2b).

According to the symmetry analysis of tilted perovskites,[15,16] the superlattice reflections at $^1/_2hk0_c$ (h, $k =$

(12) Levin, I.; Chan, J. Y.; Geyer, R. G.; Maslar, J. E.; Vanderah, T. A. *J. Solid State Chem.* **2001**, *156*, 122−134.
(13) Colla, E. L.; Reaney, I. M.; Setter, N. *J. Appl. Phys.* **1993**, *74* (5), 3414−3425.
(14) Larson, A. C.; Von Dreele, R. B. *General Structure Analysis System*; Report LAUR 86-748; Los Alamos National Laboratory: Los Alamos, NM, 1994.
(15) Glazer, A. M. *Acta Crystallogr., A* **1975**, *31*, 756.
(16) Mitchell, R. H. *Perovskites: Modern and Ancient*; Almaz Press: Thunder Bay, ON, 2002.

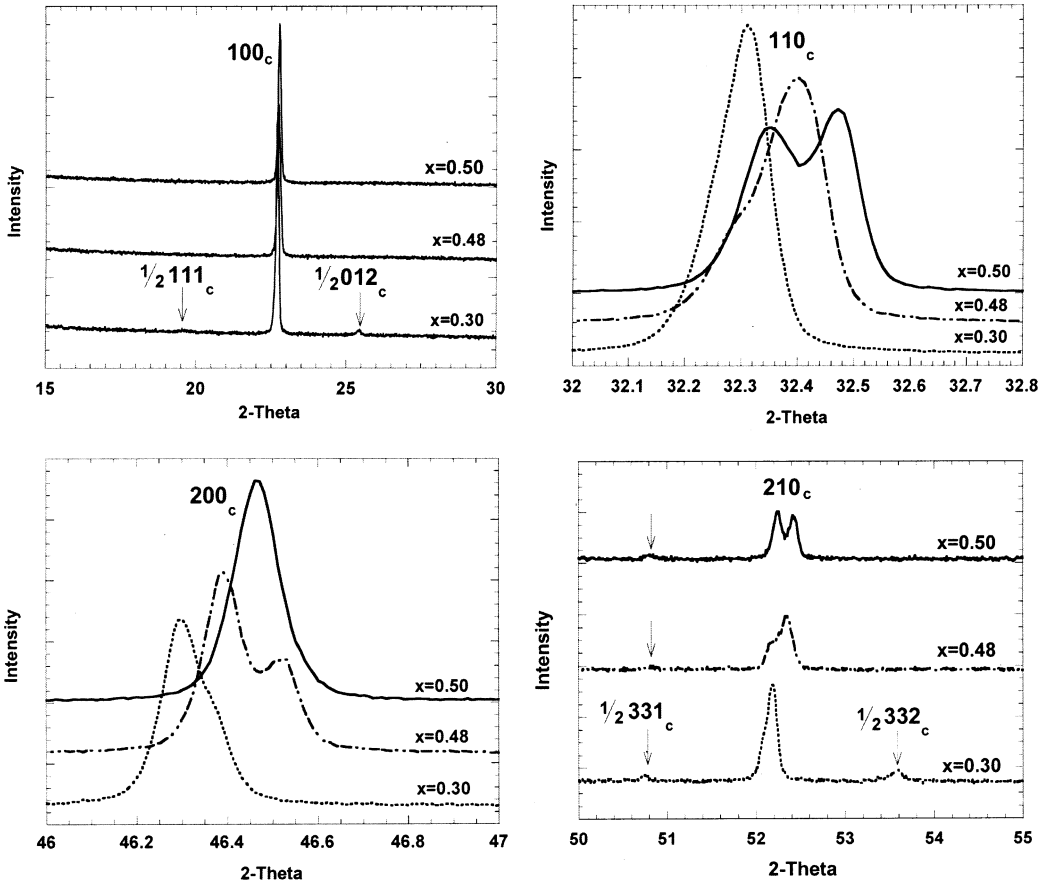

Figure 1. Representative regions of X-ray powder diffraction patterns for $x = 0.30$, 0.48, and 0.50. The fundamental reflection 110_c (b) is split for *all three* compositions (note the asymmetry for $x = 0.30$ and shoulder on the low-angle side for $x = 0.48$), whereas the 200_c reflection (c) is split for both $x = 0.30$ (note a shoulder on the high-angle side) and $x = 0.48$ compositions, but appears as a single symmetric peak for $x = 0.50$. This change in the splitting of fundamental reflections is consistent with a change from pseudo-orthorhombic to rhombohedral symmetry as x increases from 0.48 to 0.50. The superlattice reflections $^1/_2hk0$ (h, $k = 2n + 1$, $l = 2n$) and $^1/_2hk0$ (h, $k = 2n$, $l = 2n + 1$) disappear above $x = 0.30$, whereas the $^1/_2hkl$ (h, k, $l = 2n + 1$) reflections remain for all compositions.

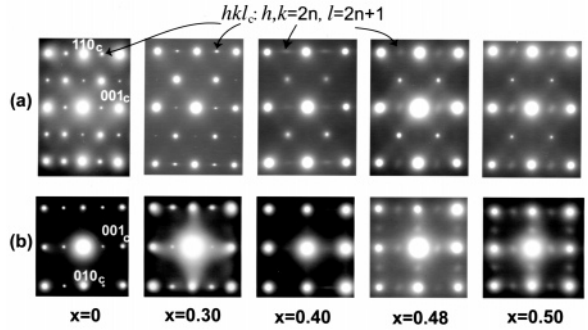

Figure 2. Selected area electron diffraction patterns recorded in the (a) $\langle 110\rangle_c$ and (b) $\langle 001\rangle_c$ zone axis orientations from single twin domains in the samples with $x = 0$, 0.30, 0.40, 0.48, and 0.50. The $^1/_2hkl_c$ (h, $k = 2n$, $l = 2n + 1$) reflections exhibit progressive weakening and streaking along the $\langle 001\rangle_c$ direction on going from $x = 0$ to $x = 0.40$. The appearance of these reflections changes drastically between $x = 0.40$ and $x = 0.48$. Note that for $x < 0.48$, the $\langle 001\rangle$ diffraction patterns from single twin domains featured one set of these reflections, whereas for $x > 0.48$ two sets were observed.

$2n + 1$) arise due to *in-phase* octahedral tilting, while those at $^1/_2hk0_c$ ($h = 2n + 1$, $k = 2n$) are associated with combined *in-phase* and *anti-phase* tilting accompanied by *antiparallel* displacements of A-cations. Some of the $^1/_2hkl_c$ (h, k, $l = 2n + 1$) reflections in the pseudo-orthorhombic $LaMg_{0.5}Ti_{0.5}O_3$ structure (011_o-type reflections, seen in Figure 2 for $x = 0$, 0.3, 0.4) are associated exclusively with cation ordering, while others (101_o-type) contain contributions from both cation ordering and anti-phase octahedral tilting (for $x = 0.48$ and 0.50 compositions the 101_o reflections could not be discerned from the 011_o using selected area electron diffraction); the contribution of Mg/Ti ordering to the intensities of the latter reflections in the X-ray diffraction patterns dominates.

Thus, the room-temperature X-ray and electron diffraction observations can be interpreted by assuming that the *in-phase* octahedral tilting diminishes with increasing x and vanishes completely for $x > 0.40$, whereas the *anti-phase* tilting is preserved across the entire solid solution range. Possible changes in the octahedral tilt system as x increases from 0.40 to 0.48 are from $a^+b^-b^-$ to $a^0b^-b^-$ (*Imma*), $a^0b^-c^-$ (*I*2/*m*), $a^-b^-b^-$ (*I*2/*a*), or $a^-b^-c^-$ ($F\bar{1}$).[17,18] Since reflection conditions (h, $k = 2n$) expected for the *a*-glide planes could not be confirmed for $x = 0.48$, the possible tilt systems for this composition were limited to $a^0b^-c^-$ and $a^-b^-c^-$. X-ray diffraction patterns for the samples with $x = 0.50$ indicated a rhombohedral distortion suggesting an $a^-a^-a^-$ tilt system for this composition. Observations of the two variants of diffuse $^1/_2hk0_c$ ($h = 2n + 1$, $k = 2n$) reflections in the single twin domain for $x \geq 0.48$ suggest that for these compositions the above reflections originate from effects other than

(17) Glazer, A. M. *Acta Crystallogr., B* **1972**, *28*, 3384.
(18) Groen, W. A.; Van Berkel, F. P. F.; Ijdo, D. J. W. *Acta Crystallogr.* **1986**, *C42*, 1472−1475.

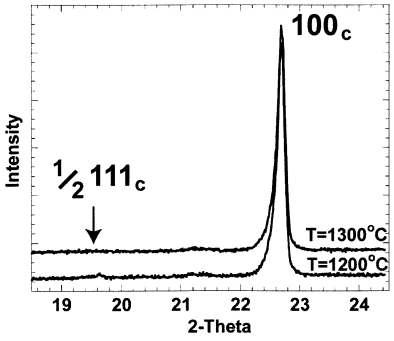

Figure 3. Lower-angle region of the X-ray diffraction powder patterns for $x = 0.30$, quenched from 1300 and 1200 °C. The sample was first annealed/quenched from 1475 °C, then annealed/quenched from the progressively lower two temperatures. The superlattice reflection at $^1/_2111$, indicative of the 1:1 Mg/Ti ordering, is absent in the diffraction pattern of the 1300 °C sample, but present after quenching from 1200 °C. The order−disorder transition occurs between these two temperatures.

octahedral tilting/La-displacements, as will be discussed below.

A series of annealing/quenching experiments demonstrated that the Mg/Ti order−disorder transition temperature, T_{ord}, decreases from above 1625 °C for $x \leq 0.1$ to $T_{ord} = 1235 \pm 35$ °C for $x = 0.3$, as inferred from the disappearance of ordering-related $^1/_2hkl$ ($h, k, l = 2n + 1$) reflections in the X-ray diffraction patterns of the samples quenched from $T > T_{ord}$ (Figure 3). While no reflections associated with B-site ordering were detected in the X-ray diffraction patterns of $x = 0.40$ samples, electron diffraction (Figure 2) revealed weak reflections at $^1/_2111_c = 011_o$, indicating that some Mg/Ti ordering is retained at this composition. For $x \geq 0.48$, the $^1/_2hkl$ reflections associated with cation ordering could not be isolated from those associated with tilting. Dark-field imaging using the $^1/_2hkl$ reflections produced no obvious contrast identifiable with the ordered domains. Considering the limited extent of cation ordering even for $x = 0.40$, we assumed that the samples with $x \geq 0.48$ were largely disordered.

Short-Range Ordering of La-Vacancies: HRTEM Imaging. High-resolution TEM imaging of samples with $x = 0.50$ was carried out to determine the origin of the diffuse $^1/_2210_c$-type reflections. The images were recorded in the $\langle 001\rangle_c = [001]_o$ projection to reveal La columns (Figure 4). Imaging of thicker areas (30−40 nm) was necessary to obtain a significant contribution of the $^1/_2210_c$-type reflections to the contrast. The resulting images consistently featured dark crosses at some of the positions corresponding to the La columns. These dark crosses exhibited visible local ordering as manifested by formation of pairs separated by ∼8 Å, and 8 Å × 4 Å rectangular arrays which gave rise to the $^1/_2210_c$-type reflections; two orthogonal variants of these pairs/arrays were observed, consistent with the two sets of $^1/_2210_c$-type reflections in the diffraction patterns. Phase contrast thickness-defocus maps were calculated for a supercell $4a_c \times 4a_c \times 2a_c$ containing two A-site columns with 50% of La-vacancies. The image simulations revealed that for thicker areas (>30 nm) close to Scherzer defocus, where the strongest contrast is observed, the columns containing La vacancies generate dark crosses similar to those observed in the experimental images (see insert in Figure 4). These

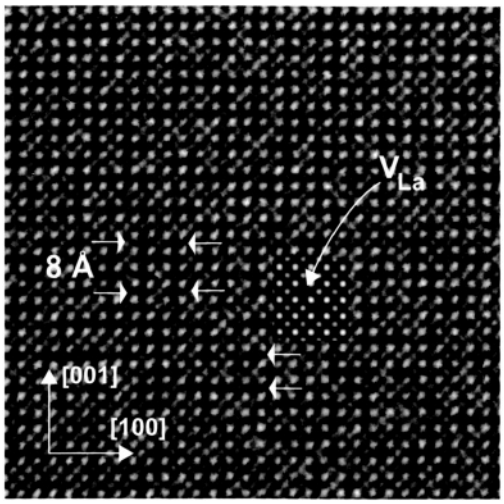

Figure 4. High-resolution structural image of $La_{0.833}Mg_{0.25}Ti_{0.75}O_3$ ($x = 0.50$) recorded in $\langle 100\rangle_c$ orientation. Dark crosses signify A-site columns containing La-vacancies. Short-range ordering of La vacancies with formation of pairs and rectangular clusters of dark-crosses is observed. The contrast calculated for the supercell $4a_c \times 4a_c \times a_c$ containing a pair of La vacancies is superimposed. The image was calculated for a thickness $t = 40$ nm and defocus $\Delta f = -32$ nm (Scherzer defocus).

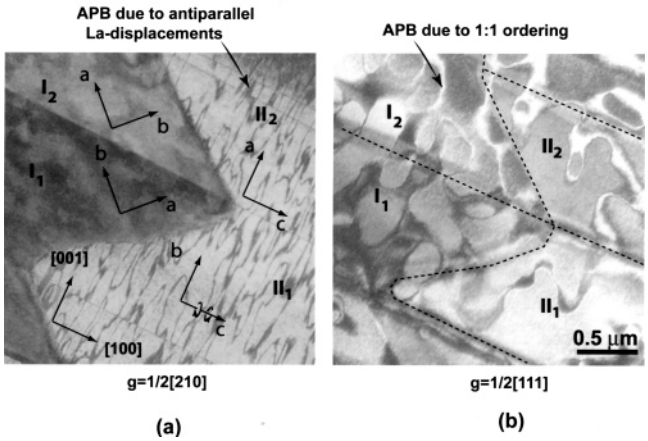

Figure 5. Dark-field images of a single grain ($x = 0.30$) recorded using superlattice reflections $\mathbf{g} = {}^1/_2[210]_c$ (a), and $\mathbf{g} = {}^1/_2[111]_c$ (b). Four twin-related domains are labeled in the images as I_1, I_2, II_1, and II_2. The anti-phase domains associated with antiparallel La displacements and 1:1 order of Mg and Ti are indicated.

results indicate the existence of short-range ordering of La vacancies for compositions with $x > 0.40$ (∼15% vacancies); this local ordering yields diffuse $^1/_2210_c$-type reflections in the diffraction patterns of compositions with $x = 0.48$ and $x = 0.50$.

Neutron Powder Diffraction. Rietveld refinements of the average structural models proposed from the electron and X-ray diffraction studies yielded satisfactory fits to the neutron powder diffraction data (See Supporting Information Figures S1−S4). The structural parameters refined for the samples $LaMg_{0.5}Ti_{0.5}O_3$ ($x = 0$, $P2_1/n$, $a^+b^-b^-$ tilt), $La_{0.9}Mg_{0.35}Ti_{0.65}O_3$ ($x = 0.30$, $P2_1/n$, $a^+b^-b^-$), $La_{0.84}Mg_{0.26}Ti_{0.74}O_3$ ($x = 0.48$, $I2/m$, $a^0b^-c^-$), and $La_{0.833}Mg_{0.25}Ti_{0.75}O_3$ ($x = 0.50$, $R\bar{3}c$, $a^-a^-a^-$) are summarized in Supporting Information Tables 1−4. Selected bond distances and bond valence sums (BVS)[19] calculated about the cations are given in Supporting Information Tables 5−8. The displacement (thermal) pa-

(19) Brese, N. E.; O'Keeffe, M. *Acta Crystallogr.* **1991**, *B47*, 192−197.

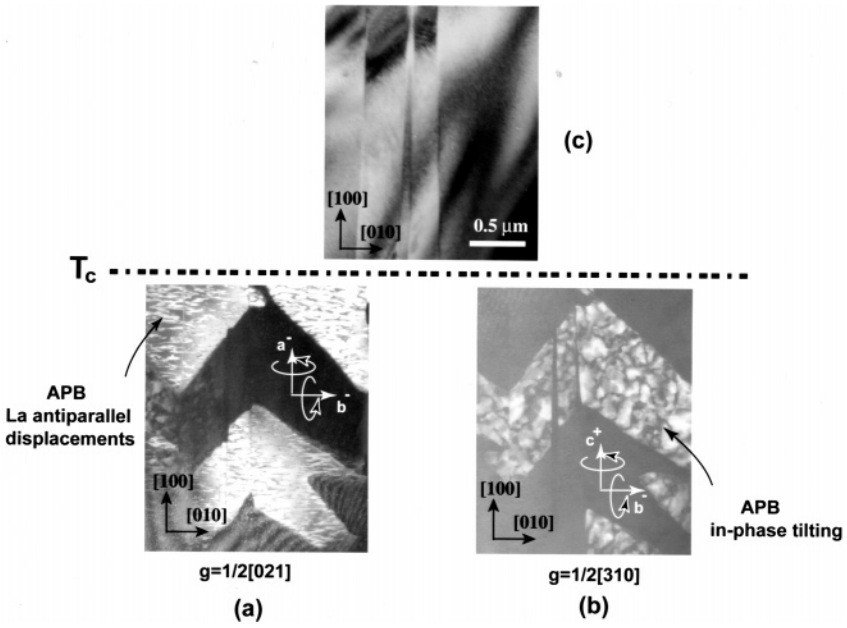

Figure 6. Dark-field images of a single grain ($x = 0.30$) recorded at (a) room temperature, and (b) 550 °C. The twin microstructure changes above $T_c \approx$ 500 °C (c) with the (110)-type twin interfaces disappearing and (100)-type interfaces preserved. The anti-phase domains associated with antiparallel La displacements and in-phase octahedral tilting also disappear above T_c.

rameters of the oxygen atoms increased considerably in the solid solutions (even for the similarly tilted average structures, i.e., $x = 0.00$ and $x = 0.30$), which can be attributed to disordered local oxygen displacements caused by the increasing concentration of La vacancies. In the present refinements, a monoclinic structure, *I*2/*m*, featuring disordered Mg and Ti and $a^0b^-c^-$ tilting was assumed for $x = 0.48$; however, a lower symmetry (triclinic) tilt system $a^-b^-c^-$ (having weak a^--tilting) cannot be ruled out for this composition. The angle of the in-phase tilting in the $P2_1/n$ $a^+b^-b^-$-tilted structure decreases from 11.4°/10.9° (the two numbers refer to the [B′O_6] and [B″O_6] octahedra, respectively) for $x = 0$ to 9.9°/9.9° for $x = 0.30$; the tilting angles were calculated[18] using the refined bond distances and lattice parameters. The tilting angle about the $\langle 110\rangle_c$ direction decreases from 12.0°/11.4° for $x = 0$ to 10.4°/10.5° for $x = 0.30$. Similar tilting angles for nonequivalent octahedra in the structure with $x = 0.30$ reflect smaller values of the 1:1 cation order parameter for this composition (see occupancies in Supporting Information Table 2) as compared to fully ordered $x = 0.0$. The anti-phase tilting angle for the $x = 0.50$ $R\bar{3}c$ structure is 9.7°.

Domain Microstructures. As mentioned above, all specimens featured assemblages of twin domains (Figure 5, 6a and b) with domain boundaries residing approximately on the $\{110\}_c$ and $\{001\}_c$ planes for $x \leq 0.48$ and on the $\{001\}_c$ planes for $x = 0.50$. For $x \leq 0.48$, these domains represent different crystallographic variants of the pseudo-orthorhombic structure $a \approx \sqrt{2}a_c$, $b \approx \sqrt{2}a_c$, $c \approx 2a_c$. The {110}-type interfaces separate variants having perpendicular *c*-axes, while the {001}-type interfaces occur between the variants having parallel *c*-axes but perpendicular *a*- and *b*-axes; these orientations of domain walls are expected for the strain-free interfaces in the orthorhombic structure.[20] For $x \leq 0.4$, in addition to twin-type domains, several types of anti-phase domains associated with octahedral tilting, antiparallel La displacements, and cation ordering were also observed (Figures 5 and 6); the scale of these domains diminished rapidly from $x = 0$ to $x = 0.4$. In particular, dark-field imaging using the $^1/_2210_c$-type reflection, which exhibited pronounced streaking along the $[001]_o$ direction, revealed a high incidence of anti-phase boundaries aligned parallel to the $(001)_o$ planes (Figures 5a and 6a). These anti-phase domains were attributed to out-of-phase antiparallel La displacements which provide a major contribution to the intensities of the $^1/_2210_c$-type reflections. Imaging the same area with the $^1/_2310_c$-type reflections (associated with in-phase tilting) revealed another set of anti-phase domains having an isotropic morphology (Figure 6b), which were attributed to regions having opposite sign of in-phase octahedral tilting. Finally, dark-field imaging using the $011_o = {}^1/_2111_c$-type reflections, associated exclusively with B-site ordering, highlighted anti-phase domains related to the out-of-phase ordering of Mg and Ti (Figure 5b).

For the $x \geq 0.48$ sample, the $^1/_2hkl$ (h, k, $l = 2n + 1$) reflections developed pronounced streaking along the $\langle 001\rangle_c$ directions, as revealed in the $\langle 103\rangle_c$ zone axis diffraction patterns (Figure 7). This streaking was attributed to a high incidence of out-of-phase boundaries (aligned parallel to the $\{001\}_c$ planes) associated with anti-phase tilting. Note that the double octahedral layers along such out-of-phase boundaries in the *anti-phase* tilted structure exhibit *in-phase* tilting about $\langle 001\rangle_c$, normal to the boundary. A single twin domain in the $x = 0.48$ sample exhibited a different extent of diffuse streaking along the two nonequivalent $\langle 100\rangle_c$ directions, consistent with $a^0b^-c^-$ or $a^-b^-c^-$ tilts. However, the presence of such $\langle 001\rangle_c$-type streaks in the $x = 0.50$ structure is inconsistent with the average rhombohedral distortion, suggesting a lower local symmetry.

(20) Sapriel, J. *Phys. Rev. B* **1975**, *12* (11), 5128−5140.

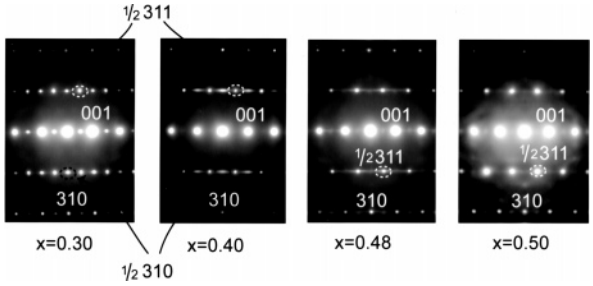

Figure 7. Selected area electron diffraction patterns recorded in the ⟨103⟩ orientation. For $x \leq 0.40$, the $^1/_2hkl$ (h, $k = 2n + 1$, $l = 2n$) reflections exhibited streaking along the ⟨001⟩ direction; these reflections are associated with in-phase tilting. In contrast, for $x = 0.48$, the $^1/_2hkl$ (h, k, $l = 2n + 1$) reflections, which are associated with anti-phase tilting, exhibit diffuse streaking.

2. Variable-Temperature Structural Behavior. The nature of the tilting phase transitions in the solid solutions $La_{1-x/3}\square_{x/3}[Mg_{(1-x)/2}Ti_{(1+x)/2}]O_3$ was inferred from the evolution of the domain microstructure upon in situ heating in TEM. In situ heating of the $x = 0.3$ sample above $T = 500$ °C resulted in a phase transition accompanied by simultaneous (i) vanishing of both $^1/_2210_c$-type and $^1/_2310_c$-type superlattice reflections along with the associated anti-phase boundaries, and (ii) disappearance of the {110}-type twin domain interfaces so that only the {001}-type domain boundaries were retained (Figure 6c); the transition was fully reversible. The diffraction observations suggested disappearance of the in-phase octahedral tilting (along with antiparallel La displacements) above $T = 500$ °C with three possible tilting transitions: $a^+b^-b^-(P2_1/n) \rightarrow a^0b^-b^-$ ($I2/m$), $a^+b^-b^-$ ($P2_1/n$)$\rightarrow a^0a^0c^-$ ($I4/m$), and $a^+b^-b^-$ ($P2_1/n$)$\rightarrow a^-a^-a^-$ ($R\bar{3}$).[17] The first sequence leaves the point group symmetry unchanged and therefore is inconsistent with the observed changes in the twin domain microstructure. In fact, the changes in the orientation of twin domain interfaces are only consistent with the $a^+b^-b^- \rightarrow a^-a^-a^-$ path because the (001)-domain boundaries, which are retained in the high-temperature phase, provide accommodation of strain in the rhombohedral ($R\bar{3}$) but not in the tetragonal ($I4/m$) structure.[20] The occurrence of a high-temperature rhombohedral $R\bar{3}$ structure featuring $a^-a^-a^-$ tilting for $x = 0.30$ is consistent with the observation of a rhombohedral $R\bar{3}c$ structure (disordered B-cations, a supergroup of $R\bar{3}$) at room temperature for $x = 0.50$; apparently, rhombohedral tilting is stabilized at lower temperatures by increasing x. Interestingly, observations of a phase transition between the $a^+b^-b^-$- and $a^-a^-a^-$-tilted structures are mostly limited to the perovskites having rare earth cations on the A-sites;[16] however, the crystal-chemical reasons for this trend remain unclear.

Variable-temperature X-ray diffraction measurements were conducted to determine the temperatures of the tilting phase transitions as a function of composition. The first phase transition on heating for samples with $x < 0.4$ was manifested by (i) disappearance of the $^1/_2hk0_c$ superlattice reflections, as observed by TEM for $x = 0.3$, and (ii) visible changes in the intensities and splitting of the fundamental reflections, as indicated by arrows in Figure 8. The temperature of this transition decreased near-linearly from $T \approx 900$ °C for $x = 0.10$ to $T \approx 50$ °C for $x = 0.48$. The abrupt redistribution of intensities for the fundamental reflections, as inferred from the patterns collected every 10 °C across the transition temperature, was consistent with the discontinuous nature of the transition $P2_1/n$ ($a^+b^-b^-$)$\rightarrow R\bar{3}c$ ($a^-a^-a^-$). Further heating resulted in a gradual disappearance of peak splitting with the ultimate transition to an untilted cubic structure. A direct rhombohedral→cubic transition was assumed as the present data were not sufficient to probe the existence of intermediate phases. Another phase transition, separating structures with $a^+b^-b^-$ and $a^0b^-b^-$ octahedral tilting, is expected to occur between $x = 0.40$ and $x = 0.48$ to account for the differences in the ambient temperature diffraction patterns for these two compositions. The tilting and Mg/Ti order−disorder phase transitions in the solid solutions $La_{1-x/3}\square_{x/3}[Mg_{(1-x)/2}Ti_{(1+x)/2}]O_3$ are summarized in Figure 9.

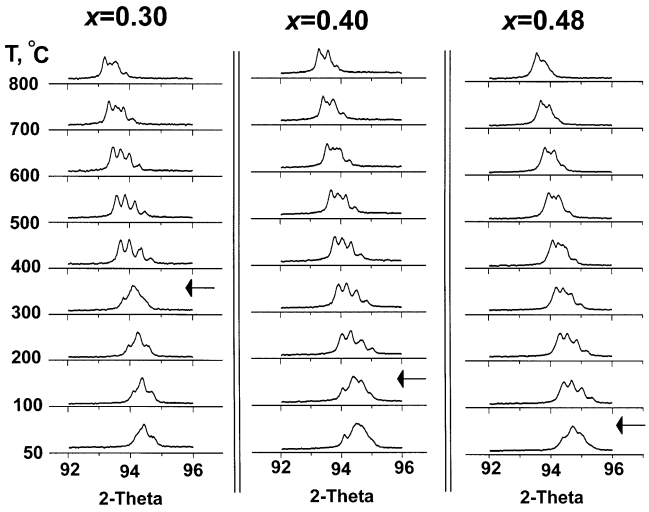

Figure 8. High-temperature X-ray powder diffraction data showing the evolution of a high-angle fundamental reflection with temperature and composition. A change in the appearance of the fundamental reflection, indicated by arrows, was attributed to a displacive phase transition between the structures exhibiting orthorhombic ($a^+b^-b^-$ for $x \leq 0.4$ and $a^0b^-c^-$ for $x = 0.48$) and rhombohedral ($a^-a^-a^-$) tilting.

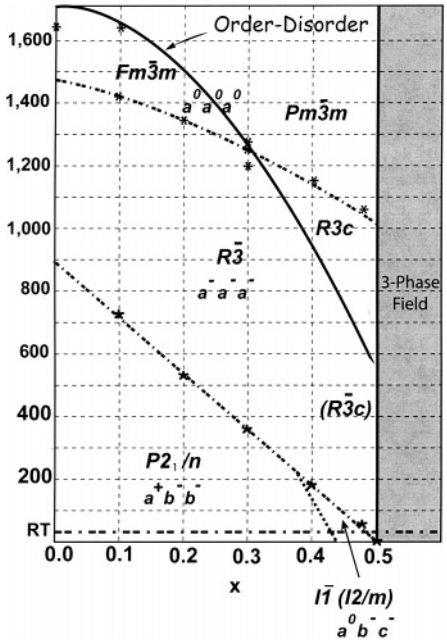

Figure 9. Diagram of ordering and tilting phase transitions in the system $(1 - x)LaMg_{0.5}Ti_{0.5}O_{3-x}La_{2/3}TiO_3$. Both order−disorder and tilting phase transitions are indicated. The experimental points are indicated using asterisks.

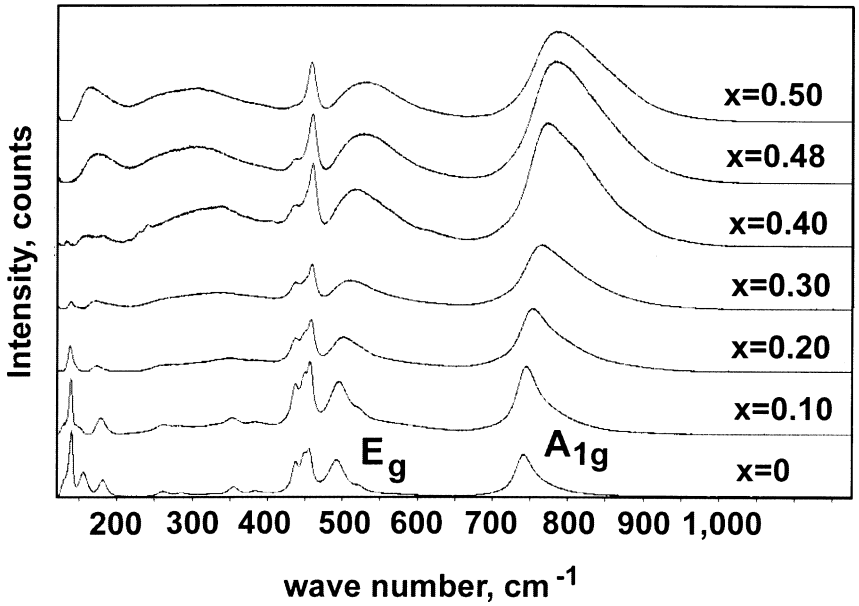

Figure 10. Background-subtracted Raman spectra for the $(1 - x)LaMg_{0.5}Ti_{0.5}O_{3-x}La_{2/3}TiO_3$ solid solutions. The E_g- and A_{1g}-like modes related to B-site ordering and associated with asymmetric and symmetric breathing of oxygen octahedra are indicated. Note the anomalous asymmetric broadening of both the E_g and A_{1g} lines with increasing x.

According to this phase diagram, the break in the slope of compositional dependences of dielectric properties reported for $x > 0.40$ correlates with the disappearance of the in-phase tilt, diminished B-site order, and the onset of short-range ordering of A-site vacancies.

3. Raman Spectra. Raman spectra collected for solid solution series are summarized in Figure 10. Factor-group theoretical analysis of monoclinic $LaMg_{0.5}Ti_{0.5}O_3$ predicts 24 Raman active modes associated with octahedral tilting and cation ordering.[21] According to recent first-principles calculations of Raman spectra for $a^+b^-b^-$-tilted double perovskites, B-site 1:1 ordering is expected to yield four intense Raman peaks with F_{2g}-, E_g-, and A_{1g}-like symmetries.[22] The higher-frequency modes A_{1g} ($\sim$800 cm^{-1}) and E_g ($\sim$550 cm^{-1}) are related to symmetric and asymmetric breathing of oxygen octahedra, respectively.[21] Both lower-frequency F_{2g}-like modes ($\sim$140 cm^{-1} and $\sim$480 cm^{-1}) are primarily related to the motion of oxygen atoms perpendicular to the B′−O−B″ bonds.

The Raman spectrum of $LaMg_{0.5}Ti_{0.5}O_3$ exhibits strong peaks at 741 and 491 cm^{-1} which can be readily identified (by analogy with other doubled perovskites) with the A_{1g}- and E_g-like breathing modes, respectively. The major effect of increasing x in the solid solutions is to progressively increase the asymmetric broadening of both the A_{1g} and E_g peaks. Additionally, the intensities of the Raman peaks at 139, 437, and 449 cm^{-1} decrease gradually with increasing x. The peaks at 139 and 449 cm^{-1} both disappear for $x > 0.40$, whereas the 437 cm^{-1} peak disappears for $x = 0.50$ only. Since the long-range B-site ordering ceases for $x > 0.40$, the peaks at 139 and 449 cm^{-1} can be tentatively attributed to the F_{2g}-like modes related to B-site ordering. The peak at 437 cm^{-1} and the strong peak at 454 cm^{-1} are likely associated with octahedral tilting.

Recent studies of the effect of B-site ordering on the Raman spectra of $CaAl_{0.5}Nb_{0.5}O_3$, which is isostructural with $LaMg_{0.5}Ti_{0.5}O_3$, revealed that the intensities of both the F_{2g} and E_g modes decreased markedly with decreasing long-range 1:1 order parameter, η, whereas the intensity of the A_{1g} mode was rather insensitive to η.[23] The width and asymmetry of all ordering-related Raman peaks varied only slightly for nearly perfectly ordered ($\eta \approx 1$) to a nearly disordered ($\eta \approx 0$) $CaAl_{0.5}Nb_{0.5}O_3$ structure.[24] Our present results for the $La_{1-x/3}\square_{x/3}[Mg_{(1-x)/2}Ti_{(1+x)/2}]O_3$ solid solutions differ from those reported for $CaAl_{0.5}Nb_{0.5}O_3$ by the anomalous asymmetric broadening of the E_g and A_{1g} modes, even for structures where significant long-range order of Mg and Ti is observed. Strongly asymmetric broadening of Raman lines is often attributed to a contribution of phonons having wave vectors $q \neq 0$; the excitation of these phonons can be caused by disorder and/or phonon confinement effects.[24] The extent of the broadening/asymmetry depends on the details of the phonon dispersion relations. First-principles calculations of phonon frequencies for $CaAl_{0.5}Nb_{0.5}O_3$ indicated a relatively small dispersion of the ordering-related Raman-active modes in this compound, consistent with minimal broadening of the Raman peaks upon increasing disorder. Phonon dispersion relations in $LaMg_{0.5}Ti_{0.5}O_3$ are unknown. Additionally, the increase in Ti content with x in the solutions $La_{1-x/3}\square_{x/3}[Mg_{(1-x)/2}Ti_{(1+x)/2}]O_3$ could modify dispersion of certain ordering-related modes. The size of the coherently diffracting anti-phase 1:1 ordered domains (0.1 μm) as deduced from dark-field images for $x = 0.3$ is too large to have any significant effect on the broadening of Raman lines. Despite this large domain size, the ordering of Mg and Ti inside each domain is highly heterogeneous because of the high concentration of Ti on the Mg sublattice; that is, each

(21) Cockayne, E. *J. Appl. Phys.* **2001**, *90* (3), 1459−1468.
(22) Prosandeev, S. A.; Wagmare, U.; Levin, I.; Maslar, J. E. *Phys. Rev. B* to be published.
(23) Levin, I.; Prosandeev, S. A.; Maslar, J. E. *Appl. Phys. Lett.* **2005**, *86*, 011919.
(24) Merlin, R.; Pinczuk, A.; Weber, W. H. In *Raman Scattering in Materials Science*; Springer-Verlag: New York, 2000; pp 1−30.

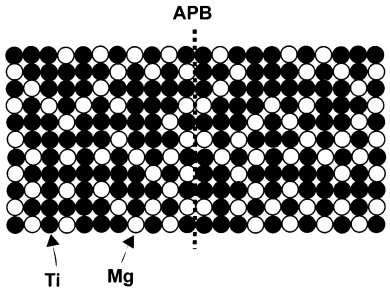

Figure 11. Schematics illustrating nanoscale heterogeneity of Mg/Ti ordering inside large anti-phase ordered domains for $x = 0.30$. The formation of nanoscale ordered regions may cause phonon confinement and the asymmetric broadening of the E_g and A_{1g} ordered-related modes observed in Figure 14. The ordered regions become increasingly isolated as the Ti concentration increases with *x*-value.

domain consists of a mixture of nanoscale regions having Ti and Mg ordered on the B-sites and those having all B-sites occupied exclusively by Ti (Figure 11). Conceivably, the correlation length of some ordering-related phonons such as the A_{1g}- and E_g-like modes is reduced as these nanosized ordered regions become increasingly isolated, causing asymmetric broadening of the Raman lines. More detailed Raman studies of these solid solutions, including those of samples having fixed compositions but varying order parameters, are needed to clarify the origin of the anomalous line broadening.

Conclusions

$(1 - x)LaMg_{0.5}Ti_{0.5}O_{3-x}La_{2/3}TiO_3$ perovskite-like solid solutions exhibit complex structural behavior with a series of octahedral-tilting phase transitions superimposed onto a B-site Mg/Ti order−disorder transition, in addition to short-range ordering of A-site vacancies. Anomalous changes in the slope of the compositional dependence of the dielectric properties reported previously for $x > 0.40$ were found to correlate with (i) vanishing of both in-phase octahedral tilting and B-site ordering, and (ii) the onset of short-range ordering of A-site vacancies. Variable-temperature diffraction studies combined with quenching experiments confirmed that the temperatures of tilting and ordering transitions decrease with increasing *x*-value; i.e., with increasing concentrations of Ti^{4+} on the B-sites and vacancies on the A-sites. The solid solutions featured a relatively uncommon tilting phase transition between the structures exhibiting orthorhombic ($a^+b^-b^-$ and $a^0b^-c^-$) and rhombohedral ($a^-a^-a^-$) tilted topologies. Raman spectra of the solid solutions exhibited previously unreported anomalous asymmetric broadening of certain lines associated with B-site ordering. This broadening was attributed to the reduced correlation length of ordering-related phonons as ordered regions become increasingly isolated with increasing Ti concentration (*x*-value). The results reported in this study reveal the complexity of the relations between the average long-range B-site order parameter, its spatial fluctuations, and Raman spectra. Detailed quantitative studies of these relations are needed to enable use of Raman spectroscopy as a routine characterization tool for B-cation ordering in complex perovskites.

Acknowledgment. Assistance provided by Virginia Miller with sample preparation is greatly appreciated.

Supporting Information Available: Figures of neutron diffraction data, and tables of occupancies, structural parameters, and bond distances and bond valence sums. This material is available free of charge via the Internet at http://pubs.acs.org.

CM040389F